The Astrophysical Journal Supplement Series, 219:1 (17pp), 2015 July doi:10.1088/0067-0049/219/1/1

A NEW CATALOG OF TYPE 1 AGNs AND ITS IMPLICATIONS ON THE AGN UNIFIED MODEL

Kyuseok Oh[1], Sukyoung K. Yi[2,3], Kevin Schawinski[1], Michael Koss[1,4], Benny Trakhtenbrot[1,5], and Kurt Soto[1]
[1] Institute for Astronomy, Department of Physics, ETH Zurich, Wolfgang-Pauli-Strasse 27, CH-8093 Zurich, Switzerland; kyuseok.oh@phys.ethz.ch
[2] Department of Astronomy, Yonsei University, Seoul 120-749, Korea
[3] Yonsei University Observatory, Yonsei University, Seoul 120-749, Korea; yi@yonsei.ac.kr
Received 2014 December 23; accepted 2015 April 24; published 2015 July 1

ABSTRACT

We have recently identified a substantial number of type 1 active galactic nuclei (AGNs) featuring weak broad-line regions (BLRs) at $z < 0.2$ from detailed analysis of galaxy spectra in the Sloan Digital Sky Survey Data Release 7. These objects predominantly show a stellar continuum but also a broad Hα emission line, indicating the presence of a low-luminosity AGN oriented so that we are viewing the central engine directly without significant obscuration. These accreting black holes have previously eluded detection due to their weak nature. The newly discovered BLR AGNs have increased the number of known type 1 AGNs by 49%. Some of these new BLR AGNs were detected with the *Chandra X-ray Observatory*, and their X-ray properties confirm that they are indeed type 1 AGNs. Based on our new and more complete catalog of type 1 AGNs, we derived the type 1 fraction of AGNs as a function of [O III] λ5007 emission luminosity and explored the possible dilution effect on obscured AGNs due to star formation. The new type 1 AGN fraction shows much more complex behavior with respect to black hole mass and bolometric luminosity than has been suggested previously by the existing receding torus model. The type 1 AGN fraction is sensitive to both of these factors, and there seems to be a sweet spot (ridge) in the diagram of black hole mass and bolometric luminosity. Furthermore, we present the possibility that the Eddington ratio plays a role in determining opening angles.

Key words: galaxies: active – galaxies: nuclei – galaxies: Seyfert – galaxies: statistics – methods: data analysis – quasars: general

Supporting material: machine-readable tables

1. INTRODUCTION

According to the unification scheme for active galactic nuclei (AGNs; Antonucci 1993; Urry & Padovani 1995), which is widely accepted in current astrophysics, different viewing angles explain the variety of phenomenological subclasses of AGNs. For example, the optical spectra of type 1 AGNs present broad permitted emission lines and narrow emission lines exposing their central nuclear region, whereas type 2 AGNs show only narrow emission lines. According to the simplest AGN unification model and its strictest interpretation, the feasibility of observing broad permitted emission lines depends solely on the angle between the observer's line of sight and the axis of an obscuring medium, often called the "dust torus."

With the aid of mega-scale surveys, such as the Sloan Digital Sky Survey (SDSS; York et al. 2000), which provide homogenous photometric and spectroscopic data, AGNs have become one of the most actively studied topics in astrophysics. In particular, studies of *obscured* AGNs showing narrow emission lines have shed light on the connection between host galaxies and their central AGNs (Kauffmann et al. 2003; Salim et al. 2007; Schawinski et al. 2007, 2009, 2010; Westoby et al. 2007; Haggard et al. 2010).

Unobscured (type 1) AGNs reveal their bright nuclear light directly, and an important task and subject of interest has been to decompose the observed light into a central nuclear component and a diffuse galaxy component. For example, the high spatial resolution Advanced Camera for Surveys on board the *Hubble Space Telescope* has been extensively used for this purpose (Sánchez et al. 2004; Ballo et al. 2007; Alonso-Herrero et al. 2008; Simmons & Urry 2008; Schawinski et al. 2011; Simmons et al. 2013) in combination with two-dimensional surface brightness fitting techniques (Peng et al. 2002).

The fraction of type 1 AGNs (among all AGNs) can act as an effective test of any model for AGN classifications and can be used to extract and constrain critical information, such as the opening angle and source luminosity, in the assumed framework. Based on a sample of high-luminosity and radio-selected broad-line AGNs, Willott et al. (2000) found a type 1 AGN fraction of 40% and a typical value for the "half-opening" angle of about 53°. The precise value of the type 1 AGN fraction has been reported to be substantially lower than this finding when low-redshift surveys of lower optical luminosity cuts are used instead (Osterbrock & Shaw 1988; Huchra & Burg 1992; Maiolino & Rieke 1995; Maia et al. 2003). This difference seems to be sensible, as more recent multiwavelength studies found a strong, positive luminosity dependence for the type 1 AGN fraction (Steffen et al. 2003; Hao et al. 2005; Simpson 2005; Hasinger 2008; Burlon et al. 2011; Assef et al. 2013).

AGNs exhibit characteristic spectral features across the electromagnetic spectrum: e.g., [O III] λ5007 optical emission lines, and mid-infrared and hard X-ray luminosity as isotropic quantities tracing the source luminosity, which are naturally employed by many type 1 AGN fraction studies. In particular, Simpson (2005) found that the type 1 AGN fraction gradually increases with L[O III] based on SDSS Data Release 2 (Abazajian et al. 2004) and hard X-ray data in the literature (Ueda et al. 2003; Grimes et al. 2004; Hasinger 2004).

[4] Ambizione Fellow.
[5] Zwicky Fellow.

Theoretical frameworks have claimed to be able to explain such a luminosity dependence for the type 1 AGN fraction. For example, the receding torus model (Lawrence 1991; Falcke et al. 1995; Hill et al. 1996; Simpson 2005) imposes a dust sublimation radius of the torus, which is directly affected by the nuclear luminosity. As the luminous central engine pushes the dust torus away, thereby increasing the torus's inner radius, the opening angle must increase if the height of the torus is fixed. This naturally explains the observed luminosity dependence of the type 1 AGN fraction.

A precise determination of the type 1 AGN fraction is obviously a key test of a model's validity. Since the AGN unified model explains the observability of both types of AGN as a consequence of obscuration induced by the geometry and the structure of AGNs, the frequency of observed type 1 AGNs indirectly constrains the model. For instance, a higher type 1 AGN fraction implies a wider opening angle, a smaller scale height for the torus, and a higher nuclear luminosity. Herein, we report on our efforts to discover new type 1 AGNs from the SDSS database to provide such a test. We describe how we found a substantial number of new type 1 AGNs and derived a more up-to-date type 1 AGN fraction. The use of the new type 1 AGN fraction places a harsh constraint on the model, and if the scheme we have used proves convincing, then it appears that an important modification to the model will be necessary. In this paper, we release a new catalog of type 1 AGNs in the nearby universe.

This paper is organized as follows. In Section 2, we describe the selection technique we used to construct the new type 1 AGN database, and we describe a simulation that quantified the detection efficiency of our method. We demonstrate our conservative scheme for type 1 selection and determine the final type 1 AGN sources, taking the simulation into account. In Section 3, we present the new type 1 AGN fraction and discuss how it may be affected by contamination caused by star formation activity. Finally, we discuss our findings and summarize our results in Section 4.

We assume a cosmology with $h = 0.70$, $\Omega_M = 0.30$, and $\Omega_\Lambda = 0.70$ throughout this work.

2. TYPE I AGN SAMPLE SELECTION

2.1. Selection Based on Broad Hα Features

The presence of unidentified type 1 AGNs in the nearby universe has been reported by Hao et al. (2005), Greene & Ho (2007), and Oh et al. (2011; also known as the OSSY catalog). In particular, Oh et al. (2011) found that the presence of broad Balmer emission lines was responsible for a very poor model fit to both the emission lines and the stellar continuum during their construction of the OSSY catalog. The authors used a flux ratio near the Hα emission line to systematically search for BLR AGNs from the SDSS DR7 galaxy database. In this work, we adopted their basic scheme but developed it further to minimize dubious detections.

The OSSY catalog provides new spectral line strength measurements for the SDSS DR7 galaxies at $z < 0.2$ ($N = 664{,}187$). By combining stellar kinematics measurements (`pPXF`; Cappellari & Emsellem 2004) and a spectral line fitting algorithm (`gandalf`; Sarzi et al. 2006), the authors released improved stellar absorption and emission line strengths, stellar velocity dispersions, and quality assessing parameters. We begin our analysis based on the OSSY catalog.

To identify the spectra showing broad Hα features,[6] we computed a ratio between the mean fluxes at two specific wavelength bands. The first narrow band (6460–6480 Å) is located near Hα but far enough from it to be free from broad Hα emission, mainly to secure the pseudo-continuum for Hα. The second narrow band (6523–6543 Å) was placed close to [N II] λ6548 to highlight the broad Hα feature. Then, we computed a flux ratio (F_{6533}/F_{6470}) based on the two bands. Figure 1 shows the flux ratio versus the signal-to-statistical-noise ratio (S/sN) of the chosen specific wavelength bands for all of the galaxies listed in the OSSY catalog ($N = 664{,}187$; $z < 0.2$). First, we used this diagram to detect Hα BLR candidates. Examples of the spectral energy distributions (SEDs) for various values of the flux ratios are illustrated in Figure 1 (surrounding panels), including the overall spectra and the Hα regions. As the flux ratio increases, broad Hα features become more prominent (see objects marked 1, 3, and 5 in order of decreasing broad Hα strength), and the same trend is visible in the higher S/sN regime (objects 2, 4, and 6). It seems clear that the flux ratio is effective for detecting Hα BLR candidates.

The 1σ demarcation line shown in Figure 1 was first applied to select type 1 AGN candidates. A total of 17% of galaxies have a flux ratio above this cut. We used `gandalf` (Sarzi et al. 2006) to fit the spectrum based on both nebular emission and stellar absorption. Our approach for analyzing the SDSS spectra can be summarized as a two-step process. First, we masked nebular emission lines and derived the stellar kinematics by directly matching the observed spectrum with stellar templates using the `pPXF` IDL program (Cappellari & Emsellem 2004). For the "stellar" templates, we used the Bruzual & Charlot (2003) stellar population synthesis models and the MILES stellar library (Sánchez-Blázquez et al. 2006). After measuring the kinematic broadening, we lifted the masking on the nebular emission lines and simultaneously fit stellar continuum and emission lines using Levenberg–Marquardt minimization (Markwardt 2009).[7]

The standard `pPXF` and `gandalf` procedures generally work well on normal galaxies, but a more elaborate consideration is necessary for type 1 AGNs. For example, for type 1 AGNs only, we adopted a wide masking width of 12,000 km s^{-1} for broad Balmer lines (Hα, Hβ, Hγ, and Hδ) and 1200 km s^{-1} for narrow emission lines prior to measuring stellar kinematics. In addition, we imposed an initial assumption of a large width, 1000 km s^{-1}, for broad Balmer component fitting. We implemented a single broad Gaussian component for each Balmer line. As demonstrated in the middle panels of Figure 2, these prescriptions were effective for decomposing the broad (Hα) and narrow (Hα, [N II] λ6548 and [N II] λ6584) components around the broad Hα region.

Following these routines, we measured the FWHM, flux, and amplitude-over-noise ratio (A/N)[8] of all of the lines listed in the OSSY catalog. Our selection criteria for type 1 AGN candidates are as follows:

1. $0.00 < z < 0.20$;
2. FWHM of broad Hα > 800 km s^{-1};
3. A/N of broad Hα > 3.

[6] Broad Hα is also a signature of supernovae, but it is known to be rare (Filippenko 1997).

[7] `pPXF` and `gandalf` use the MPFIT IDL routine provided by Craig Markwardt at http://cow.physics.wisc.edu/~craigm/idl/.

[8] A/N is defined by the ratio between the Gaussian amplitude of the emission line and the dispersion of the continuum residual of the given spectrum.

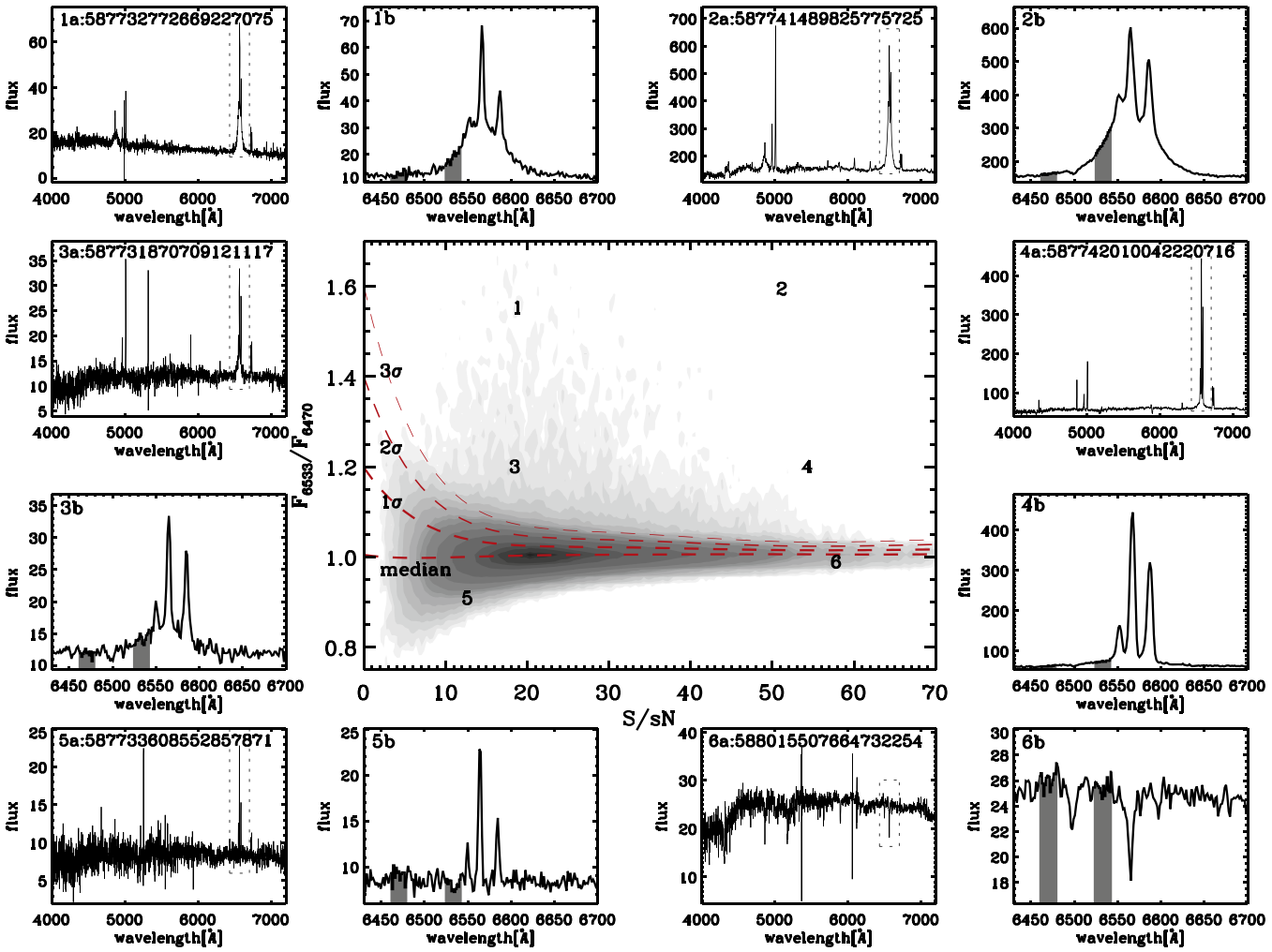

Figure 1. Flux ratio (F_{6533}/F_{6470}) distribution vs. S/sN. The demarcation lines in the central panel are shown as red dashed lines. The three lines indicate 84.1%, 97.7%, and 99.8% distributions. Example spectra represented by the numbered markings in the central panel are shown in the surrounding panels, with two small sub-panels for each object. The surrounding panels marked with "a" on the top left side show the overall shape of the spectrum, whereas the panels marked "b" show the Hα region. Each object is labeled in sub-panel "a" by its SDSS ObjID. Black solid lines indicate the observed spectrum. The two narrow bands that define the flux ratio are shaded gray. Four spectra (numbered from 1 to 4) are chosen as type 1 AGN candidates out of six examples by the demarcation lines. Flux has the unit 10^{-17} erg s^{-1} cm^{-2} Å^{-1}.

The redshift limit is constrained by the wavelength of the red end of the pseudo-continuum around Hα. We chose a cut for FWHM(Hα) that was slightly lower than the one more widely used, 1000 km s^{-1} (Vanden Berk et al. 2006; Schneider et al. 2010; Stern & Laor 2012), hoping to detect even weaker BLR AGNs. As a result, we found 9671 (8.6%) type 1 AGN candidates among the 111,824 sources that satisfied the 1σ cut shown in the central panel of Figure 1. Of these 9671, only 120 were of FWHM(broad Hα) < 1000 km s^{-1}, and hence the choice of the 800 km s^{-1} cutoff instead of the more typical 1000 km s^{-1} cutoff influenced our results and conclusions little.

2.2. Test of the Selection Scheme

The selection process described above relies on the specific flux ratio as a proxy to the broad Hα feature. To verify our approach and measure the detection efficiency, that is, its completeness and purity, we conducted a simulation by generating mock spectra, each with an artificially broadened Hα component.

The basis of the mock spectra was 110 star-forming galaxies with narrow emission lines: 10 galaxies randomly chosen from 11 S/sN bins. To secure a wide range of amplitude for Hα, we used the spectra of actively star-forming galaxies with star formation rate (SFR) > 0.5 $M_{\odot}$ yr^{-1} that were identified by the BPT diagnostics diagram (Baldwin et al. 1981) and the Kennicutt law (Kennicutt 1998). We then added broad-line components by varying two parameters, Gaussian peak and FWHM, while the center of the Gaussian was fixed at 6562.8 Å. The peak of the Gaussian was fractionally scaled by the amplitude of the narrow Hα emission line ($A_{\mathrm{H}\alpha}$) in 19 steps, namely, by 1% increments from 1% to 10% and a 10% increment from 10% to 100% in $A_{\mathrm{H}\alpha}$. The FWHM of the broad Hα line was varied between 50 and 15,000 km s^{-1} in 50 km s^{-1} increments. For reference, the typical range of the FWHM(Hα) of star-forming galaxies is 50–350 km s^{-1} within the 2σ level. In total, 627,000 ($110 \times 19 \times 300$) mock spectra were generated, as summarized in Table 1.

Figure 3 shows the flux ratios versus S/sN (left panel) and FWHM (right panel) for the simulated galaxies. In the left panel, the galaxies with low FWHMs (dark red color) were

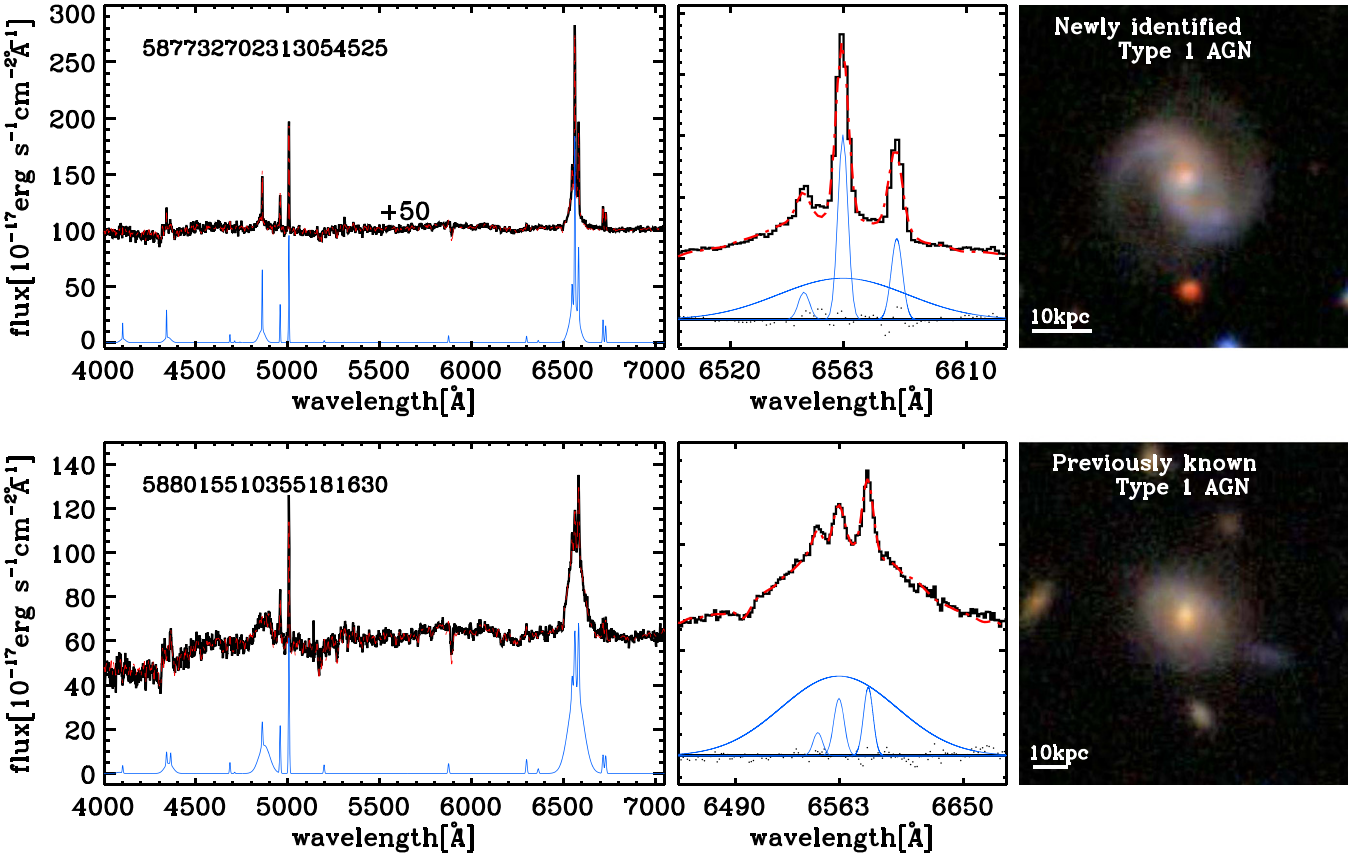

Figure 2. Example spectra with SDSS *gri* composite images for a newly identified type 1 AGN (top) and a previously known type 1 AGN from the SDSS pipeline (bottom). Left and middle panels present the overall spectra and their Hα regions, respectively. Black lines indicate the observed spectra, and red dashed lines include stellar continuum fits. Note that the observed spectrum and the fit in the top panel are shown with an offset in the ordinate for clarity (+50 in flux unit). Detected emission lines are shown in the left panels as blue lines. In particular, broad Hα components are shown in the middle panels, as well as other narrow emission lines. Dots in the middle panels show the residuals.

Table 1
Simulation Designs

Components	Range	Increment	No. of Bins
S/sN[a]	5–55, >55	5	11
FWHM	50–15,000 (km s^{-1})	50	300
Peak[b]	0.01 × $A_{H\alpha}$[c] –0.09 × $A_{H\alpha}$	0.01	9
	0.1 × $A_{H\alpha}$ – 1.0 × $A_{H\alpha}$	0.1	10

Note. In total, 627,000 mock galaxies were generated.
[a] Average S/sN from four continuum bands (4500–4700, 5400–5600, 6000–6200, 6800–7000 Å).
[b] Peak of the Gaussian.
[c] Amplitude of the narrow Hα.

generally found below the 1σ demarcation line and/or had low S/sN. As the color grids show, our 1σ cut for recovering BLRs with a large value of FWHM (blue color) seems effective, although it still suffers from contaminants such as objects with noise fluctuations or a broad Hα component that is too shallow. We will discuss how these contaminants can be removed in the next section. The right panel of Figure 3 shows that the highly star-forming galaxies having only narrow emission lines obviously occupy the region of low flux ratio (<1.1) and low FWHM (<500 km s^{-1}). Below the FWHM of 500 km s^{-1}, the mock galaxies have almost the same flux ratios as narrow emission line galaxies, which means that it is not easy to distinguish between weak type 1 AGNs and star-forming galaxies. On the other hand, the flux ratio of the mock galaxies begins to spread out significantly for FWHM > 1000 km s^{-1}.

Detection efficiency (completeness and purity) can be measured by assuming that a BLR AGN has FWHM (broad Hα) > 800 km s^{-1}. Completeness is defined as the fraction of mock BLR AGNs recovered by the procedure (i.e., the σ cut). Purity describes the fraction of BLR AGNs among all of the galaxies selected by a σ cut. Table 2 lists the completeness and purity of BLR AGNs for three choices of σ cut. As higher σ cuts are applied, completeness decreases but purity increases.

Figure 4 illustrates that the completeness (color key) of our selection method based on the flux ratio of the broad Hα component is mainly determined by the broad Hα luminosity (ordinate). We used this completeness distribution to find BLR AGN candidates most economically. We first located the locus of 90% completeness pixels in the diagram. As most of the pixels above this locus satisfy the completeness of 90%, the total completeness when using this 90% cut is in practice much greater than 90%. Roughly 21% (2052 out of 9671) of the BLR AGN candidates (by the 1σ criterion) were below the 90% demarcation line and thus were missed by this scheme.

2.3. Selection Based on the Broadening around [N II]λ6584

So far, we have described our selection criterion based on the broad Hα feature, but there are still complexities. For instance,

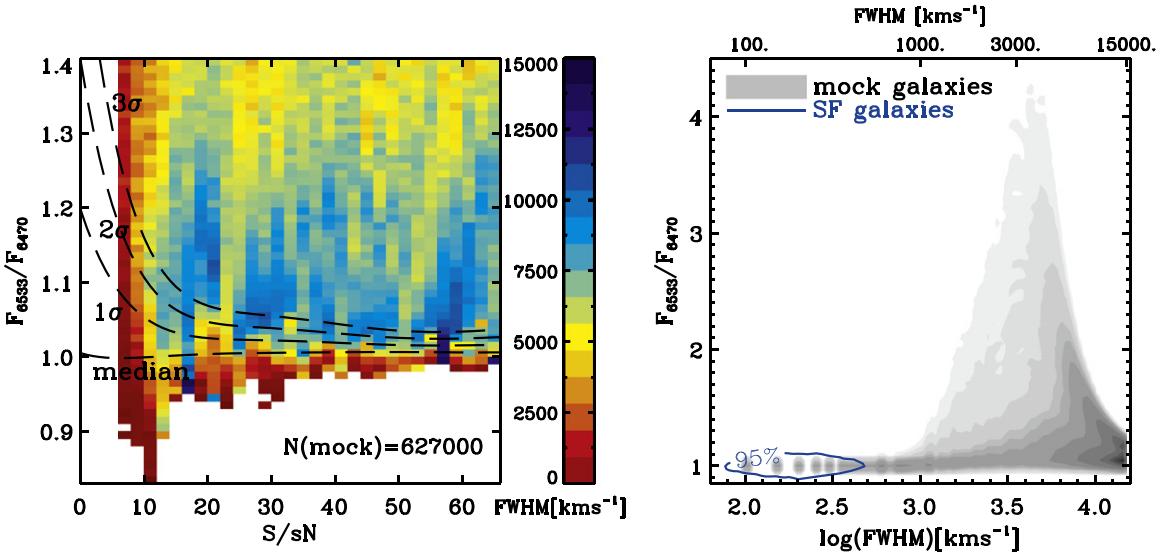

Figure 3. Flux ratio distribution with respect to S/sN (left) and FWHM (right) for the simulated galaxies. In the left panel, color grids and the corresponding color bar represent the mean FWHM. In the right panel, FWHMs measured for the actively star-forming galaxies are indicated by a blue contour (95%), while the values for the mock spectra are indicated by achromatic filled contours.

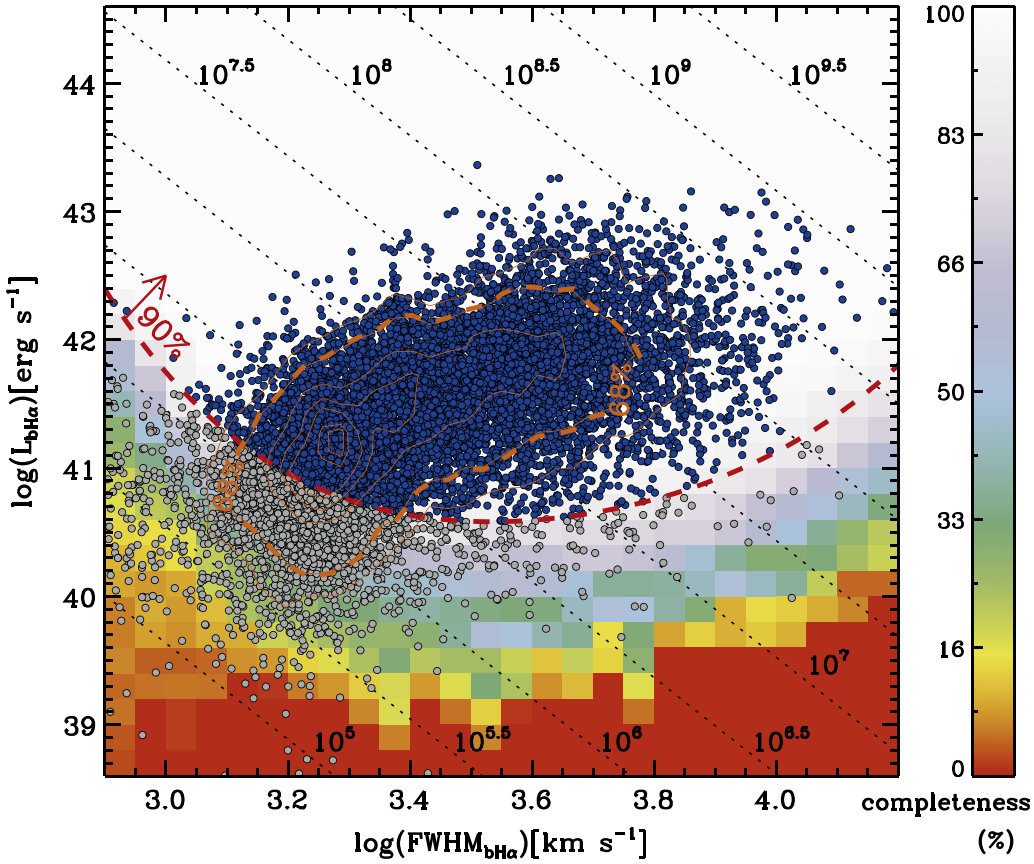

Figure 4. Luminosity vs. FWHM for broad Hα components. Completeness derived from a simulation is indicated by the underlying color grid. Labeled black dotted lines represent $M_{\rm BH}$ in units of solar mass following the formulae developed by Greene & Ho (2005). The red dashed curve indicates the demarcation used to choose type 1 AGN sources based on a 90% completeness criterion. The type 1 AGNs ($N = 7619$) selected by the 90% completeness cut are shown as blue filled dots; excluded points ($N = 2052$) below the curve are shown as gray filled dots.

an extremely shallow broad Hα component can technically be classified as a type 1 AGN as long as it satisfies our conditions of A/N and FWHM, but not without doubt. For another example, the credibility of type 1 classification for border-line objects with FWHM(Hα) just over 800 km s^{-1} can be doubted because it is difficult to measure accurately the width of such a marginally broad Hα component, especially in the midst of strong neighboring narrow emission lines ([N II] λ6584).

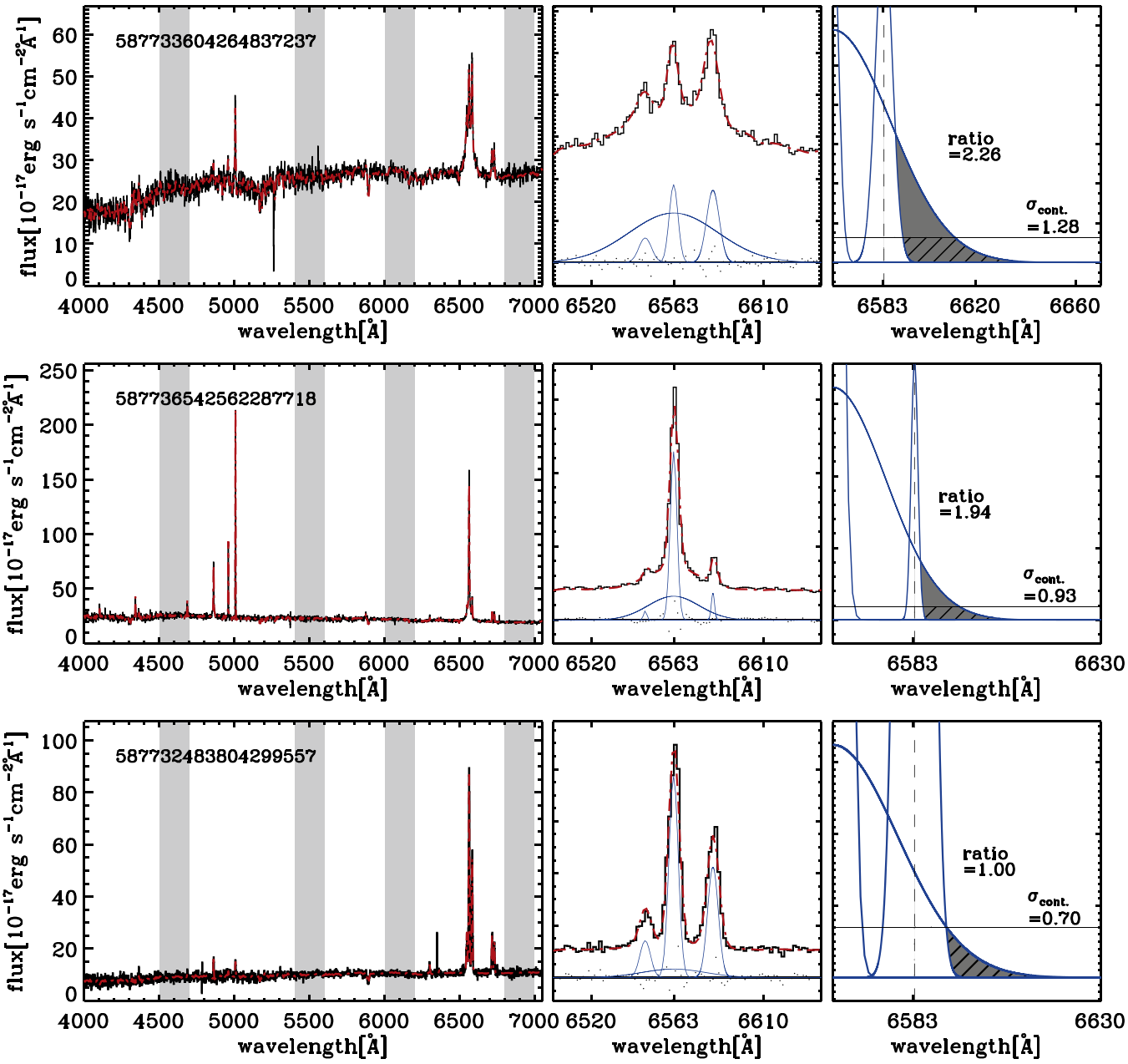

Figure 5. Example spectra illustrating the conservative selection criterion based on areal excess. The overall spectra are shown in the left panels, with SDSS ObjID labels included in the top left. Black and red lines, respectively, indicate the observed spectrum and our fit. The regions that are used to measure the averaged continuum dispersion are shaded gray. The middle panels present the detected [N II] λ6548, narrow Hα, broad Hα, and [N II] λ6584 emission lines (blue Gaussians) and their residuals (black dots). The right panels enlarge the middle panels, comparing the measured broad Hα exceeding [N II] λ6584 (gray shades) to the level of the continuum dispersion (hatched regions with black horizontal lines). The areal excess, that is, the ratio between the gray shaded and the hatched regions, is marked, as is the level of the continuum dispersion, $\sigma_{cont.}$.

Table 2
Detection Efficiency for Each σ Cut

σ Cut[a]	No. of Mock Galaxies	No. of Mock BLRs	Completeness[b] (%)	Purity (%)
$>1\sigma$	547,495	543,052	91.49	99.19
$>2\sigma$	515,939	514,562	86.69	99.73
$>3\sigma$	487,943	487,512	82.13	99.91

Notes.
[a] σ cut marked in the central panel of Figure 1.
[b] Number of all mock broad-line AGNs (FWHM > 800 km s^{-1}) = 593,560.

Having carried out a sophisticated spectral fit for each galaxy spectrum and having determined decomposed broad Hα properties as a result, we were able to perform a more stringent type 1 classification than has been carried out so far. We compared the area of the broad Hα component in question with the noise level of the observed continuum. The area of broad Hα beyond [N II] λ6584 to longer wavelengths can be used as an alternative measure of FWHM for the broad Hα feature. Meanwhile, the area defined by the dispersion (measurement uncertainty) of the continuum can be used as a control parameter. Figure 5 provides an illustration with

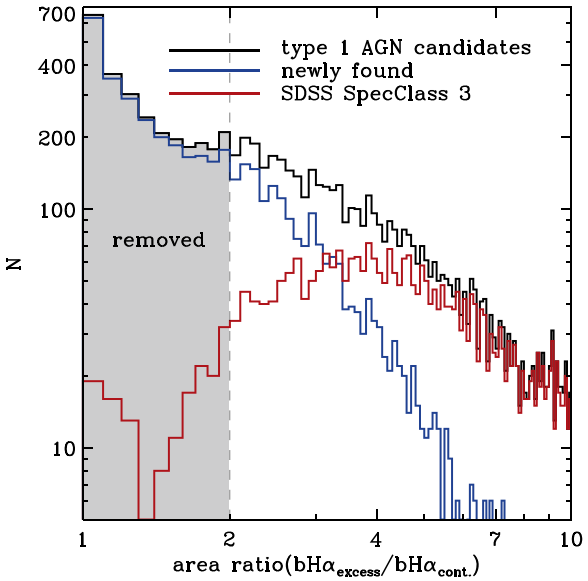

Figure 6. Histograms of area ratio for all type 1 AGN candidates (black), newly discovered type 1 AGNs (blue), and SDSS *SpecClass* 3 sources (red). The new selection criterion, area ratio >2, is marked using a vertical dashed line; it removes 2066 dubious candidates (gray shaded area).

Table 3
Detection Efficiency for Each σ Cut after Applying Areal Ratio

σ Cut	No. of Mock Galaxies	No. of Mock BLRs	Completeness (%)	Purity (%)
$>1\sigma$	547,495	484,791	81.68	88.55
$>2\sigma$	515,939	476,341	80.25	92.33
$>3\sigma$	487,943	463,475	78.08	94.99

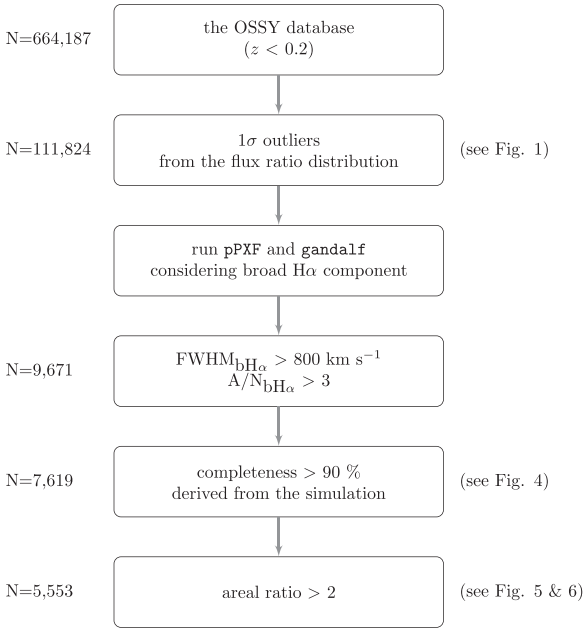

Figure 7. Flowchart of the type 1 AGN selection.

example spectra. The right panels demonstrate how we assess the broad Hα component (gray shaded area) that surpasses the level of the continuum dispersion (hatched area), which is marked as $\sigma_{\rm cont.}$. As an additional type 1 AGN criterion, we take the areal ratio of the broad Hα over the measurement

Table 4
Detection of *SpecClass* 3 Sources

		N	%
Total detected[a]		4125	100.00
	after flux ratio cut	4079	98.89
	after $A/N_{bH\alpha}$ and $FWHM_{bH\alpha}$ cut	3969	96.22
	after completeness cut (>90%)[b]	3921	95.05
	ater areal excess cut (>100%)[c]	3718[d]	90.13
missed		407	9.87
Description on the Sources That Failed Flux Ratio Cut			
	only narrow emission lines	19	41.30
	absence of spectral information	11	23.91
	maybe broad-line AGNs	10	21.74
	passing $A/N_{bH\alpha}$ and $FWHM_{bH\alpha}$ cut	(10)	(21.74)
	passing completeness cut (>90%)	(8)	(17.39)
	passing areal excess cut (>100%)	(5)	(10.87)
	asymmetric bump on Hα	3	6.52
	non-emission lines	2	4.35
	unknown spectrum	1	2.17

Notes.
[a] Number of all detected *SpecClass* 3 sources chosen from the flux ratio analysis at $z < 0.2$.
[b] See Section 2.3 and Figure 4.
[c] See Section 2.4 and Figure 5.
[d] Number of *SpecClass* 3 sources in the final catalog.

uncertainty around [N II] λ6584 greater than 2. The application of this new cut removed 3940 controversial type 1 AGN candidates (Figure 6). Table 3 lists the completeness and purity for each σ cut after implementing areal ratio analysis. As is the case with any other criterion, some of the objects removed in this step are likely to be true type 1 AGNs. However, we felt it necessary to apply this additional criterion to construct a more robust list of type 1 AGN candidates.

By using the completeness (>90%) and areal ratio (>2) arguments, we identified 5553 type 1 AGN candidates. It should be noted that the majority (91.3%) of the type 1 AGN candidates below the 90% completeness cut in Figure 4 were eliminated using the areal excess test, confirming the effectiveness of the completeness test as a filtering scheme. The flowchart in Figure 7 shows the number of objects that survived each selection. The broad nature of the Hα emission line of type 1 AGNs eluded our initial attempt to measure their strengths. Perhaps for the same reason, many (38%, 700 out of 1835) of our newly discovered type 1 AGNs are not included in the MPA-JHU catalog.[9] Hereafter, our analysis is based on these 5553 sources.

We list the measured properties of these sources and the estimated quantities with a designation flag in Table 9. We used the formula developed by Greene & Ho (2005) that depends on the line width and luminosity of the broad Hα to estimate black hole mass. We assumed the bolometric luminosity by adopting the relationship developed by Heckman et al. (2004; $L_{\rm bol} \approx 3500\,L[{\rm O\,III}]$). The cross-matched flag shows that 456 type 1 AGNs (8.2%) and 2954 (53.2%) sources in our catalog are

[9] http://www.mpa-garching.mpg.de/SDSS/DR7/

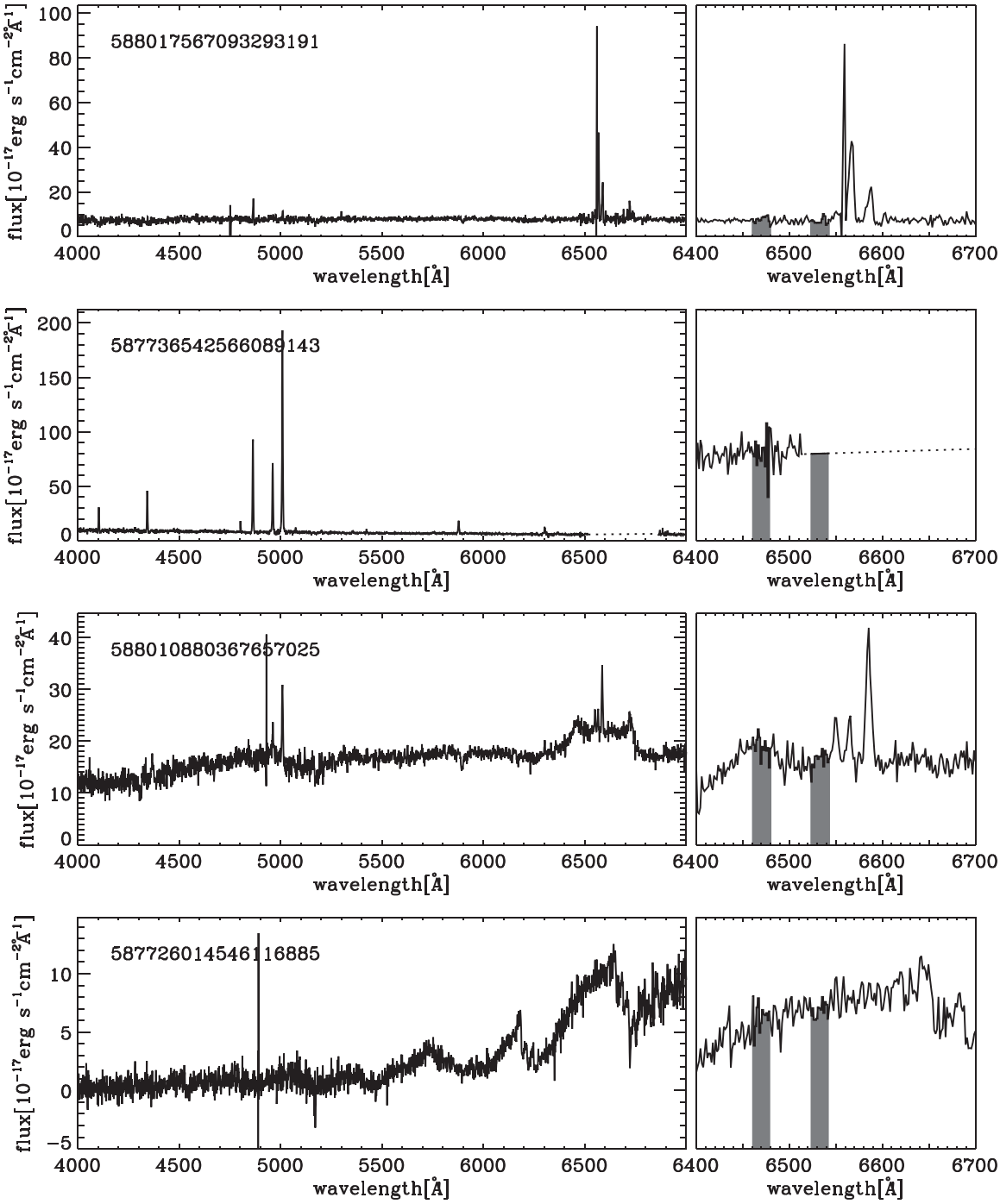

Figure 8. Spectra of example *SpecClass* 3 sources below the 1σ demarcation line, for a narrow emission line galaxy (top), an incomplete spectrum near Hα (upper), an asymmetric bump feature (lower), and an M-type star (bottom). Right panels show the Hα region; the two narrow bands that define the flux ratio are shaded gray.

found in Hao et al. (2005) and Greene & Ho (2007), respectively.

2.4. SDSS SpecClass = 3 Objects

SDSS DR7 provides a spectroscopic classification of galaxies: *SpecClass*. Broad-line AGNs, especially at low redshift, are flagged *SpecClass* = 3 when the observed spectrum satisfies the following criteria: the FWHM of *any* emission line is greater than 1000 km s^{-1}, the height of the emission line is at least 3 times higher than its noise (equivalent to our condition of A/N > 3), and the equivalent width of the line is larger than 10 Å. In total, there are 4125 *SpecClass* 3 sources at $z < 0.2$. Galaxies not showing broad emission lines are classified as *SpecClass*2.

We tried applying our type 1 AGN selection technique on *SpecClass* 3 objects; Table 4 summarizes our results. To begin with, 4079 out of 4125 objects passed our flux ratio test. Then, 3969 of the remaining objects passed the A/N and FWHM cuts, and 3718 (90.13%) passed the final areal excess test. Overall, our technique rejected roughly 10% (407 out of 4125) of the objects.

We further describe why some of the SDSS *SpecClass* 3 objects are not classified the same way in our analysis based on

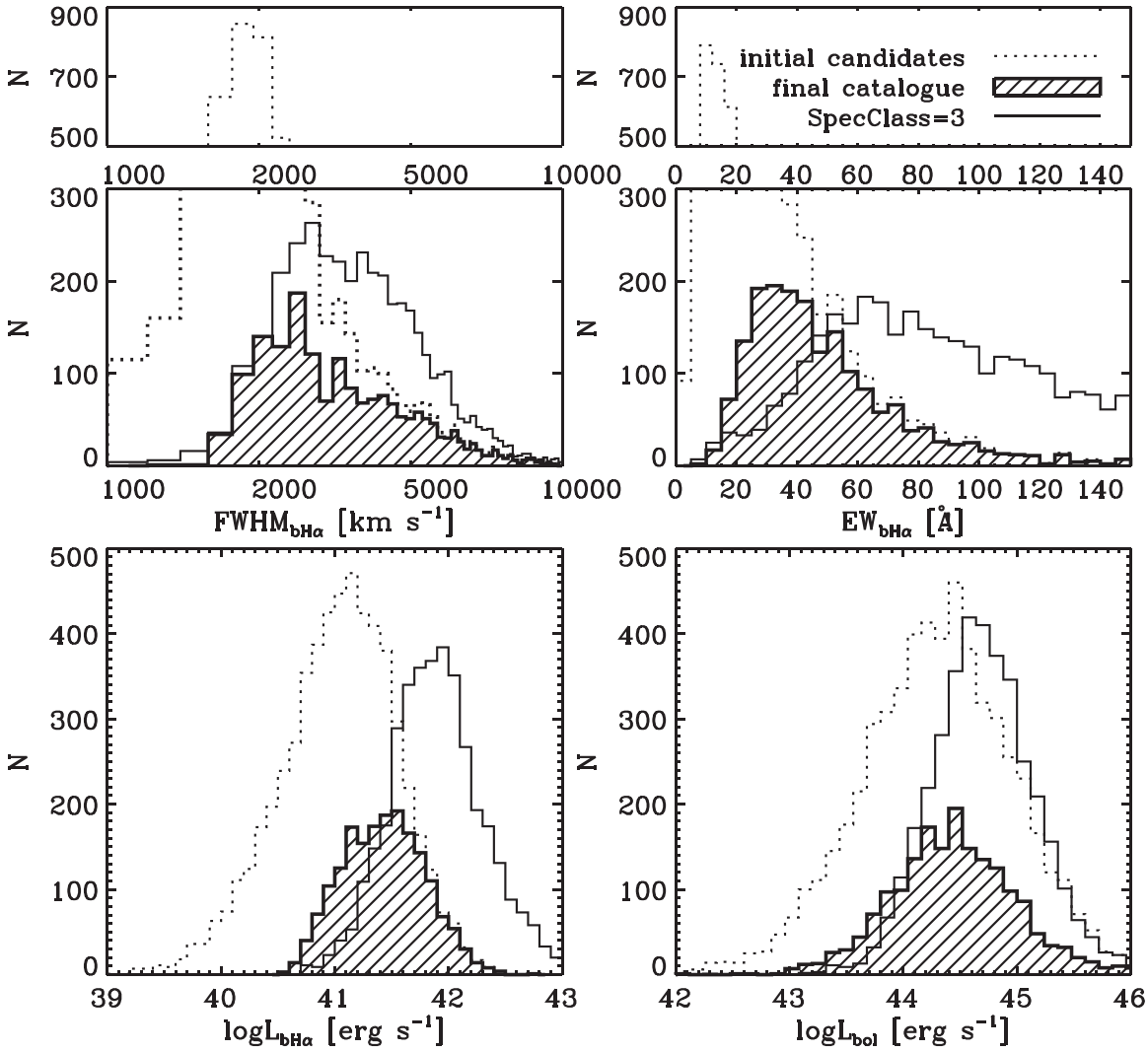

Figure 9. Histograms of FWHM$_{bH\alpha}$, EW$_{bH\alpha}$, log$L_{bH\alpha}$, and logL_{bol} for newly discovered type 1 AGNs (hatched area; see Section 2.3), *SpecClass* 3 sources (solid lines), and all type 1 AGN candidates (dotted) chosen by measuring the flux ratio F_{6533}/F_{6470} (see Section 2.1).

a subsample of the objects that were excluded by the first and most important step of our scheme, the flux ratio test. By performing additional spectral fitting to the 46 (4125–4079) sources that failed to pass the 1σ cut from the flux ratio distribution, we found that 11 objects have empty spectral bins around Hα (see Figure 8, second row). Hence, our technique could not be feasibly applied to these objects. In the majority of the other 35 missed objects (25 out of 35), we could not detect any notable broad features; the top row of Figure 8 shows such an example. Of the 46 missed objects, 10 passed our A/N and FWHM tests of Hα and thus may have broad Hα components. However, 2 of the 10 failed to pass our 90% completeness test, and another 3 failed to pass the areal excess cut test; overall, only 5 out of 10 passed all of our tests. Similarly, our technique could not be effectively applied to three objects because their spectrum around Hα appeared asymmetric and uneven (see Figure 8, third row). Finally, one object had a spectrum that did not appear to be an ordinary galaxy spectrum, making it difficult to fit this spectrum with a combination of template stellar (population) spectra (Figure 8, bottom row). Table 4 summarizes the statistics of the *SpecClass* 3 sources.

Figure 9 presents the distributions of the widths and luminosities of the broad Hα component for the newly discovered type 1 AGNs (hatched area) and *SpecClass* 3 sources (solid line). The new sources show broad Hα widths (FWHM$_{bH\alpha}$) comparable to those of the *SpecClass* 3 sources. On the other hand, the characteristic luminosity (i.e., the peak of the distribution) and the equivalent width of their broad Hα components seem lower by a factor of a few than those of the *SpecClass* 3 objects, where the bolometric luminosity is derived from $L_{bol} \approx 3500L[\mathrm{O\,III}]$ (Heckman et al. 2004). Hence, the newly discovered objects are mostly *low-luminosity* type 1 AGNs.

2.5. Chandra X-ray Data

A strong X-ray flux is one of the prominent and characteristic features of an AGN because an accretion disk surrounding a central black hole produces X-ray emission (Fabian et al. 1989). Relativistic electrons from the corona in the vicinity of the accretion disk scatter the lower-energy photons radiated from the accretion disk. As a result, the lower-energy photons receive more energy from the electrons (inverse Compton scattering), and this process produces an X-ray spectrum with a power-law continuum (Haardt & Maraschi 1991; Zdziarski et al. 2000; Kawaguchi

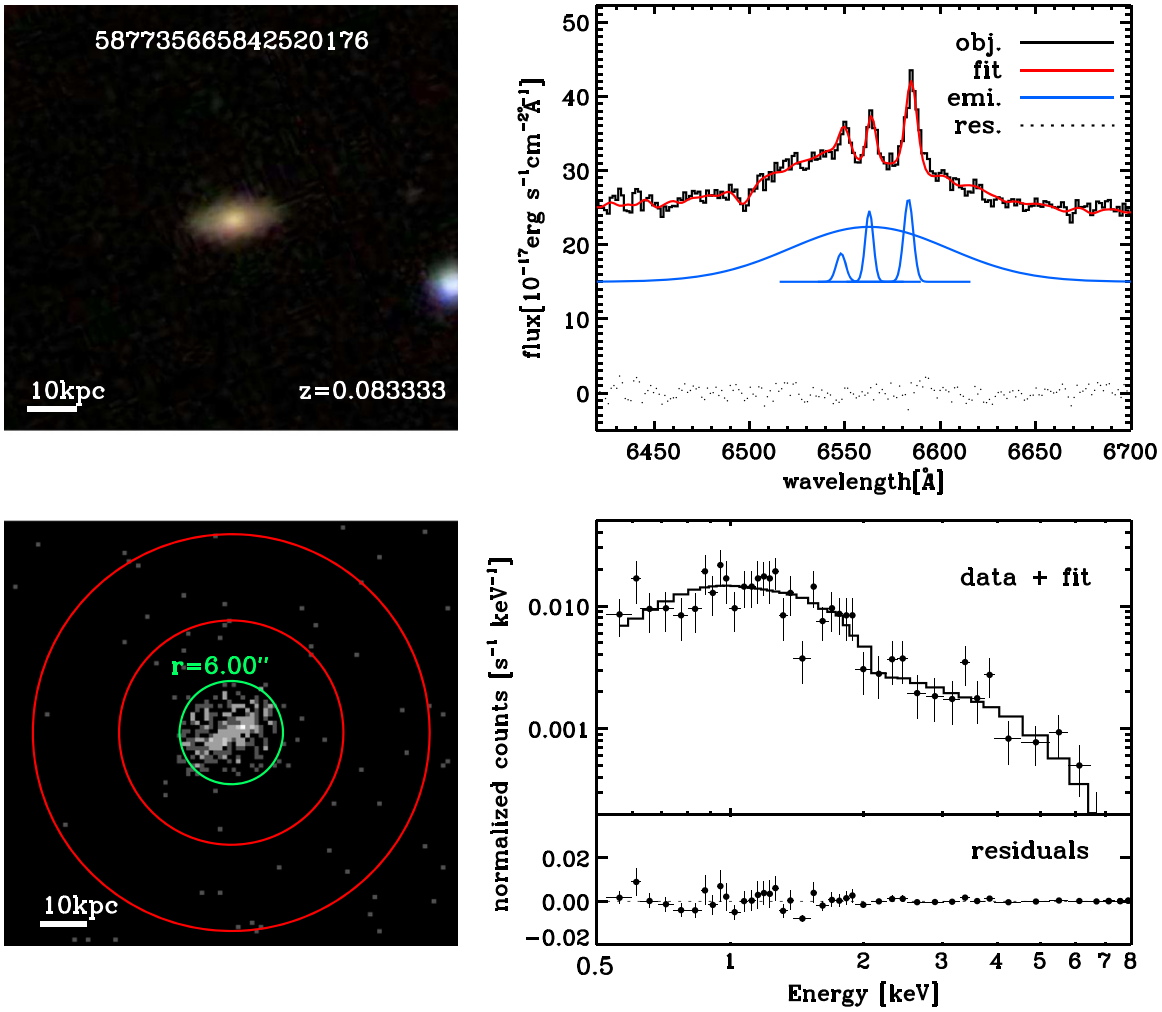

Figure 10. Example *Chandra* X-ray data (obsid = 2779) and model fit, with the SDSS *gri* composite image and our spectral fit. Top left: SDSS *gri* composite image. Top right: observed spectrum (black), our fit (red), detected emission lines (blue) including broad components, and residuals (black dots). Note that the detected emission lines are arbitrarily shifted toward the *y*-axis for clarity. Bottom left: *Chandra* X-ray image, including source (green circle) and background (red annulus) markers. Bottom right: extracted data with the applied fit vs. energy (top) and residuals (bottom).

Table 5
X-Ray Fitting Strategies

Count	Fitting Prescription N_H [cm^{-2}][a]	Γ[b]
$\leqslant$50	10^{20} fixed[c]	1.9 fixed
50 < count < 100	10^{20-24} variable	1.9 fixed
$\geqslant$100	10^{20-24} variable	1.5–2.5 variable

Notes.
[a] Hydrogen column density.
[b] X-ray photon index.
[c] The value is fixed during spectral fit.

et al. 2001). Thus, strong X-ray emission is considered to be evidence of the presence of an AGN.

We utilized the *Chandra* Source Catalog (Evans et al. 2010) and archival *Chandra* X-ray data to identify X-ray sources among our AGN candidates. We downloaded the matched X-ray images from the *Chandra* archive and applied a 10′ matching radius. Through visual inspection of X-ray images of their optical counterpart, we found 84 X-ray sources among the type 1 AGN samples. The X-ray recovery rate (1.5%) was very low, mainly because X-ray sky coverage was much narrower (by a factor of 25) and depth was much shallower compared to the SDSS optical survey.

We used the *Chandra* Interactive Analysis of Observations (CIAO) v4.6[10] and XSPEC v12.8.1 g software[11] (Arnaud 1996) to reprocess the *Chandra* X-ray data and perform a spectral fitting analysis. We manually aligned the coordinates to the actual image center and determined the source aperture, A_s (green circle in Figure 10), by reading off the value from the pipeline relation between the off-axis angle and the aperture size suggested. The applied aperture ($\overline{A_s}$ = 11.2 kpc, σ_{A_s} = 10.0 kpc) generally covers the whole galaxy ($\overline{\mathrm{PetroR90}_r}$ = 12.2 kpc, $\sigma_{\mathrm{PetroR90}_r}$ = 6.2 kpc, where PetroR90$_r$ is the radius containing 90% of Petrosian flux in the *r* band), while some nearby sources represent the central part. Then, we used `specextract` with `psfcorr` in CIAO, which incorporates an energy-dependent aperture correction (average enclosed energy fraction is 85%). We set the sky background to an annulus with a 10″ width (or 13″) away from the center when $A_s < 5''$ (or $A_s \geqslant 5''$). We grouped all spectra

[10] http://cxc.harvard.edu/ciao/
[11] http://heasarc.nasa.gov/xanadu/xspec/

Table 6
X-Ray Properties of Type 1 AGNs

SDSS ObjID	Obsid[a]	R.A.[b] (degree)	Decl.[b] (degree)	z	Counts	Count Rate (Count s^{-1})	$\log L_{2-10\,keV}$[c] (erg s^{-1})	Note[d]
587738372207476987	3784	121.94200	21.23800	0.14215	230	0.012	$42.76^{+0.08}_{-0.06}$	3
587735665842520176	2779	211.12100	54.39800	0.08333	318	0.022	$42.56^{+0.06}_{-0.06}$	*N*
587725551741370430	2033	143.96500	61.35300	0.03933	332	0.007	$41.36^{+0.04}_{-0.04}$	*N*
587741602568798223	4695	184.53300	28.17600	0.17773	449	0.045	$43.30^{+0.05}_{-0.05}$	*N*
587725551197683729	7146	124.83400	50.00700	0.13969	171	0.022	$42.77^{+0.09}_{-0.09}$	3
587729774220738649	9557	210.21899	−1.75300	0.14878	1662	0.034	$42.92^{+0.02}_{-0.02}$	*N*
587731521745518723	827	140.28600	45.64900	0.17448	4617	0.246	$44.16^{+0.02}_{-0.01}$	3*p*
587729653959033079	887	249.20200	41.02900	0.04737	287	0.004	$41.28^{+0.05}_{-0.07}$	*N*
587735696453009410	1623	220.76199	52.02700	0.14121	2851	0.190	$43.86^{+0.02}_{-0.02}$	3*p*

Notes.
[a] *Chandra* observation ID.
[b] *Chandra* J2000 coordinates.
[c] Errors are estimated with the 90% confidence region for a single interesting parameter.
[d] Discriminating flag for the newly identified type 1 AGNs ("*N*") and the previously confirmed sources ("3"). The notation "*p*" indicates a photon pileup fraction greater than 10%.

(This table is available in its entirety in machine-readable form.)

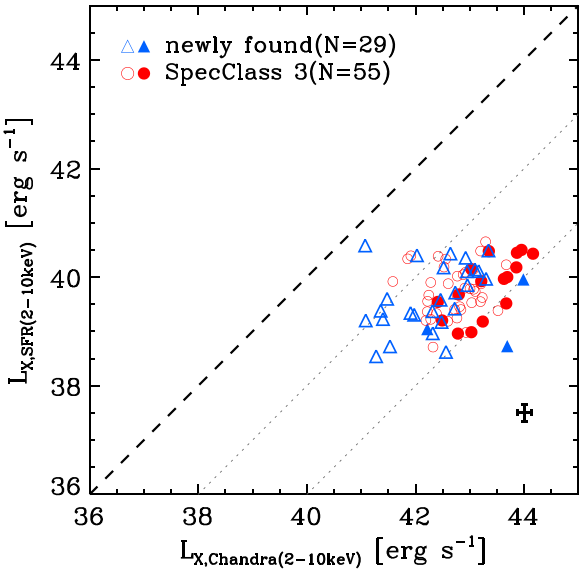

Figure 11. Comparison of 2–10 keV X-ray luminosity between measurements ($L_{X,Chandra}$) and SFR-inferred estimates ($L_{X,SFR}$). Newly discovered type 1 AGNs and *SpecClass* 3 sources are shown as blue triangles and red circles, respectively. Those objects having more than 10% photon pileup fraction are shown with filled blue triangles (3 out of 29) and filled red circles (16 out of 55). The black cross at the bottom right indicates the mean error for all sources. The central dashed line is a one-to-one fiducial line. Two additional dotted lines are shown to facilitate comparison.

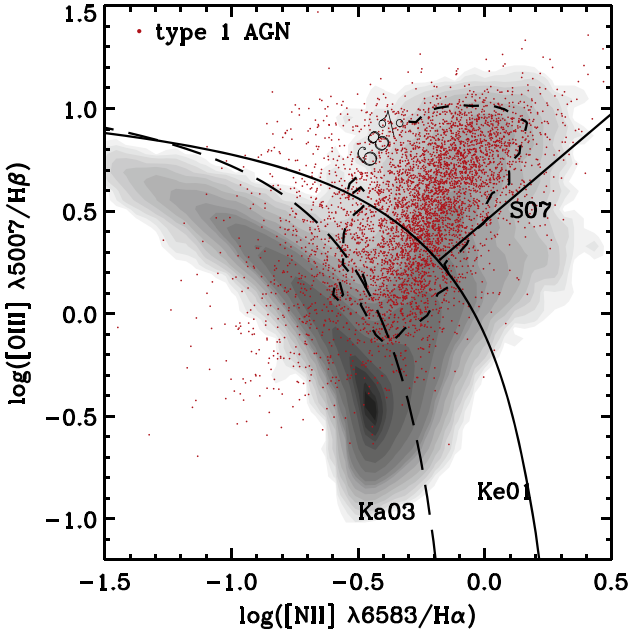

Figure 12. BPT diagnostic diagram for type 1 AGNs (red dots). Emission-line galaxies with A/N cut (>3 for [N II] λ6584, Hα, [O III] λ5007, and Hβ; $N \approx$ 180,000) chosen from the entire OSSY catalog are shown with filled contours. The dashed contour indicates 68% distribution for type 1 AGNs.

with a minimum of 1 count per bin and applied the Cash statistic (Cash 1979) with the assumption of the Poisson distribution to achieve spectral fitting for low-count spectra. XSPEC command `statistic cstat` applies the W statistic (Wachter et al. 1979) for the unmodeled background spectra. We performed spectral fitting by applying the photo-electric absorption model and power law (`phabs*pow` in XSPEC) in the rest-frame energy range between 0.5 and 8.0 keV. Table 5 gives a detailed prescription for the spectral fitting procedure, Table 6 describes the X-ray properties measured on these sources, and Figure 10 shows an example result.

Apart from AGNs, there are other luminous X-ray sources such as high-mass X-ray binaries, young supernova remnants, and hot ionized interstellar medium resulting from star formation activity. In-depth studies have proposed a correlation between the global SFR and X-ray luminosity across the whole galaxy (Grimm et al. 2003; Ranalli et al. 2003; Grimes et al. 2005; Lehmer et al. 2010; Mineo et al. 2011). In particular, Ranalli et al. (2003) showed the following linear relationship between 2–10 keV X-ray luminosity and SFR

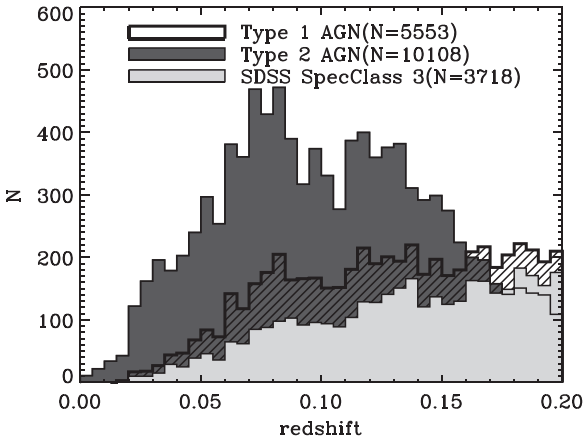

Figure 13. Histograms of type 1 (thick line) and type 2 AGNs (dark gray area) with respect to redshift; the type 1 AGN samples include 3,718 *SpecClass* 3 sources (light gray area). The hatched area represents the newly discovered type 1 AGNs.

based on 23 bona fide star-forming galaxies:

$$\mathrm{SFR}\left[M_{\odot}\mathrm{yr}^{-1}\right] = 2.0 \times 10^{-40} L_{2-10\,\mathrm{keV}}. \quad (1)$$

We can also estimate SFR using Hα narrow emission line strength, following Kennicutt (1998), and then derive the 2–10 keV X-ray luminosity ($L_{\mathrm{X,SFR}}$) using this equation. Figure 11 compares $L_{\mathrm{X,SFR}}$ and $L_{\mathrm{X,Chandra}}$ for the 84 type 1 AGNs for both the newly disocvered type 1 AGNs (blue triangles) and the SDSS *SpecClass* 3 sources (red circles). Fluxes (horizontal axis) are calculated from the best-fit model. The *Chandra* X-ray luminosities ($L_{\mathrm{X,Chandra}}$) are two to four orders of magnitude higher than the SFR-inferred estimates ($L_{\mathrm{X,SFR}}$), robustly confirming that our new candidates are indeed AGNs.

Regarding the photon pileup fraction of our *Chandra* sources, we performed an investigation based on the count rate. We explicitly marked the sources with filled symbols in Figure 11 if the object has a count rate per second greater than 0.07, which corresponds to a photon pileup fraction greater than 10%. The loss of photon count underestimates X-ray luminosity (horizontal axis of Figure 11). There are 19 sources (out of 84) that show a photon pileup fraction greater than 10%, and their intrinsic X-ray luminosity would be found farther away from the fiducial line in Figure 11. Hence, photon pileup does not change our conclusion that 84 X-ray sources are powered by AGNs.

2.6. Type 2 AGN Selection

Based on the OSSY catalog (N = 664,187, $z < 0.2$), we chose the type 2 AGNs from the Seyfert region of the BPT AGN diagnostic diagram (Baldwin et al. 1981). We used the theoretical maximum starburst model of Kewley et al. (2001) and the empirical star formation curve derived by Kauffmann et al. (2003) as demarcation lines. To discriminate low-ionization nuclear emission line regions from Seyfert AGNs, we used the empirical demarcation of Schawinski et al. (2007). In addition, we used the criterion A/N > 3 as a threshold to secure the statistical significance for the narrow emission lines ([N II] λ6584, narrow Hα, [O III] λ5007, and Hβ) used in the diagnostics (Figure 12). As a result, we selected 10,108 type 2 AGNs at $z < 0.2$. The BPT AGN diagnostics diagram for type 1 AGNs is presented in Figure 12. The overall distributions of type 1 and type 2 AGNs versus redshift are shown in Figure 13.

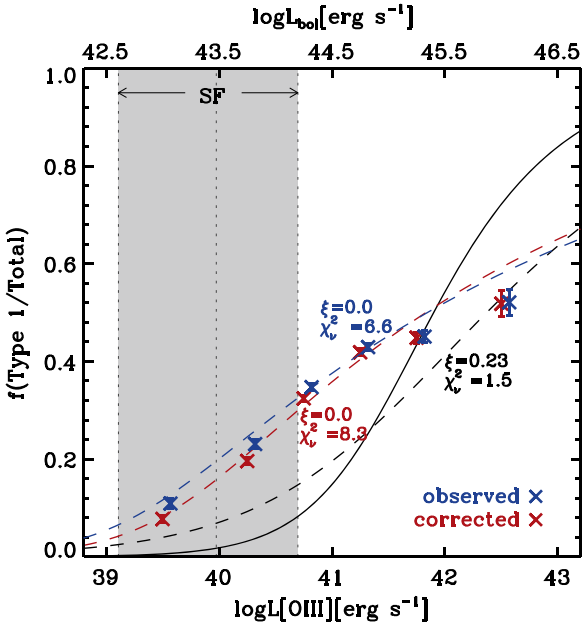

Figure 14. Type 1 AGN fraction with respect to [O III] λ5007 luminosity. Bolometric luminosity is shown on the top axis, following $L_{\mathrm{bol}} \approx 3500\,L$[O III] (Heckman et al. 2004). Blue crosses and error bars show the observed type 1 AGN fraction. Red crosses and error bars show the type 1 AGN fraction estimated by statistically correcting for the dilution of observed type 2 AGNs due to star formation. The gray band shows the range of L[O III] of star-forming galaxies sampled so that their stellar mass distribution matched that of type 2 AGNs. Vertical dotted lines denote the median and 95% distributions. The black solid curve represents the standard receding torus model proposed by Simpson (2005). The black dashed curve indicates the modified receding torus model, which allows us to vary the height of the torus according to the nucleus luminosity with $\xi = 0.23$. The best fits for the observed (blue) and dilution-corrected (red) data points are shown as blue and red dashed lines, including ξ. Note that the error bars are barely visible due to their small magnitudes, except for the highest L[O III] bin.

3. TYPE 1 AGN FRACTION

By combining both types of AGN, we obtained the type 1 AGN fraction, namely, the number ratio between type 1 AGNs and all AGNs as a function of [O III] λ5007 luminosity and bolometric luminosity (Figure 14, Table 7). The observed type 1 AGN fraction (blue crosses in Figure 14) increases with L [O III]. This trend is generally consistent with predictions based on the receding torus model, but does not match closely: the luminosity dependency of the type 1 AGN fraction is steeper at low L[O III] and becomes flattened at high L[O III] bins compared to the "standard" model (black solid curve) that was derived from the fit to the type 1 AGN fraction from SDSS DR4. Simpson (2005) noted that the degree of match (to the old data) improved when the height of the torus was modified to depend on the nucleus luminosity in the form of $h \propto L^{\xi}$ (black dashed line) with $\xi > 0$. In the "modified" scheme, the sublimation radius of a dust torus gradually increases with the nuclear luminosity L[O III]. In this framework, the type 1 fraction is described as $f_1 \equiv N_1/N_{\mathrm{tot}} = 1 - [1 + 3(L/L_0)^{1-2\xi}]^{-\alpha}$, where α is set to be 0.5. In Simpson's formulation, the best fit is to reproduce $f_1 = \alpha$ for a combination of (L_0, ξ); this yielded $L_0 = 42.37$ erg s^{-1} and $\xi = 0.23$ for the reduced χ^2_{ν} of 1.5. The

Table 7
The Observed Type 1 AGN Fraction with the Dilution-corrected Data

$\log L_{\rm bol}$ (erg s^{-1})	$\log L$[O III] (erg s^{-1})	f(type 1 AGNs/total) (%)	f(type 1 AGNs/total)$^{a}_{\rm corrected}$ (%)	$N_{\rm type1AGN}$	$N_{\rm type2AGN}$	$N^{\rm corrected\ b}_{\rm type2AGN}$
42.5–43.5	39.0–40.0	10.90 ± 0.98	7.72 ± 0.71	110	899	416
43.5–44.0	40.0–40.5	23.08 ± 0.86	19.60 ± 0.75	553	1843	426
44.0–44.5	40.5–41.0	34.71 ± 0.67	32.42 ± 0.63	1778	3344	363
44.5–45.0	41.0–41.5	42.92 ± 0.71	41.86 ± 0.70	2084	2772	123
45.0–45.5	41.5–42.0	45.08 ± 1.16	44.83 ± 1.15	833	1015	10
45.5–46.5	42.0–43.0	52.09 ± 2.64	51.80 ± 2.63	187	172	2

Notes.
[a] Dilution-corrected type 1 AGN fraction, which is described in Section 3.1.
[b] Number of dilution-corrected type 2 AGNs.

modified model does not seem to be consistent with our new data, however. We revisit this issue in the next section.

Challenges remain in accurately defining the true type 1 fraction. For example, as discussed in previous sections, our type 1 selection scheme probably excludes some true type 1 AGNs as a consequence of finding robust type 1 AGNs. In this sense, our type 1 fraction may be considered a lower limit. On the other hand, the number of type 2 AGNs is also uncertain. Most notably, we have selected type 2 AGNs only from the Seyfert category based on the BPT diagnostics (see Section 2.5). However, it is likely that there are some type 2 AGNs hidden in the composite and even the star-forming categories. We now attempt to discover them and to include them in our estimation of the type 1 fraction.

3.1. Dilution Correction on the Optical Lines of Type 2 AGNs

Our analysis starts by setting up two groups of galaxies at $z < 0.2$: "emission-line" galaxies ($N \sim 200,000$) and star-forming galaxies ($N \sim 150{,}000$) from the OSSY catalog. Emission-line galaxies obviously include star-forming galaxies. We use only those galaxies with A/N > 3 for all four lines of [N II] λ6584, Hα, [O III] λ5007, and Hβ that are used in the BPT diagnostics. Assuming that the amount of emission flux coming from star formation depends mainly on the stellar mass, we matched every emission-line galaxy with a BPT-selected star-forming galaxy with the same stellar mass within a 5% tolerance level, based on the stellar mass listed in the MPA-JHU catalog. The size (number of galaxies) of the pool of galaxies with (roughly) the same stellar mass for each galaxy used in our test, which depends strongly on stellar mass itself and the shape of the stellar mass function, is roughly 3400 (median).

This match between an emission-line galaxy and a star-forming galaxy solely based on stellar mass is invalid when it is performed on a single galaxy because, even for the same stellar mass of galaxies, SFR can vary widely, resulting in different emission line strengths. However, when this exercise is applied to numerous galaxies, and as long as there is no serious bias of SFR in any sense in the sample, the method can be considered largely valid. We subtracted the emission line strength of the star-forming galaxy from the emission-line galaxies for all four narrow lines, and we adjusted the position of each galaxy in the BPT diagram based on its residual line strengths. Note that we have done this for all of the emission-line galaxies, including star-forming galaxies themselves.

After removing the star-forming components in the emission lines, 550 star-forming galaxies were moved to the Seyfert region of the BPT diagram, as shown in Figure 15. This does not mean that there is a significant AGN component in all of these star-forming galaxies. Instead, this arose from the randomness of the choice of our star-forming galaxy as a subtraction. Likewise, after this subtraction, many star-forming galaxies ended up having negative emission lines, again as a result of the randomness of the process. Hence, we decided to ignore this result.

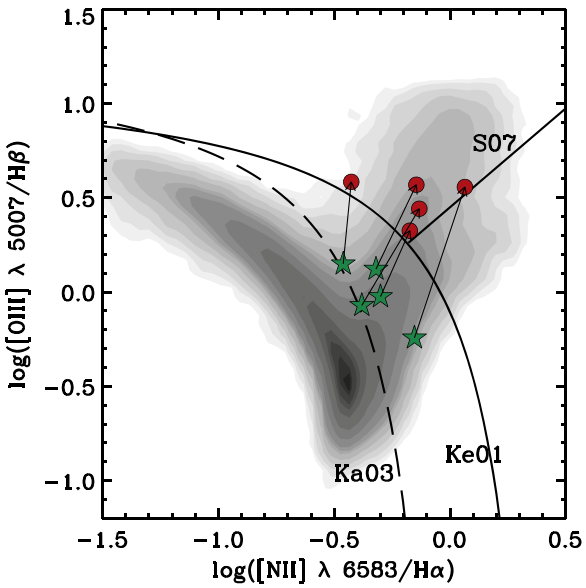

Figure 15. BPT diagnostic diagram with five randomly chosen examples. All emission-line galaxies at $z < 0.2$ having A/N > 3 on [N II] λ6584, Hα, [O III] λ5007, and Hβ are represented by filled contours. Composite objects (green stars) are shown that were moved to the Seyfert region (red circles) by the procedure described in the main text.

The light emitted by "composite" galaxies is believed to include the contributions of both star-forming and AGN activities, and thus this exercise makes more sense when applied to these galaxies; applying this process moved 1374 composite galaxies from the composite region to the Seyfert region (Figure 15). Again, some of these moves may be a result of applying an unfair star formation correction due to the randomness of our process. This yielded a total of 11,482 (10,108 + 1374) type 2 AGNs. The new type 1 AGN fraction that resulted from this "dilution" correction is shown in Figure 14 using red crosses and error bars.

The analysis is not complete because we randomly chose and considered emission-line fluxes of star-forming galaxies that

Table 8
Type 1 AGN Fraction as a Function of Eddington Ratio

	$\log(M_{BH}/M_{\odot})$			$\log L_{bol}$[a]		
$\log\lambda_{Edd}$	6.5–7.0	7.0–7.5	7.5–8.0	43.2–44.0	44.0–44.8	44.8–45.6
−3.0–2.0	0.07 ± 0.05	0.14 ± 0.04	0.25 ± 0.04	0.24 ± 0.03	0.30 ± 0.06	0.14 ± 0.13
−2.0–1.5	0.14 ± 0.03	0.20 ± 0.02	0.30 ± 0.02	0.21 ± 0.02	0.35 ± 0.02	0.43 ± 0.07
−1.5–1.0	0.25 ± 0.02	0.29 ± 0.01	0.41 ± 0.01	0.24 ± 0.01	0.34 ± 0.01	0.58 ± 0.02
−1.0–0.5	0.43 ± 0.01	0.44 ± 0.01	0.51 ± 0.02	0.28 ± 0.02	0.44 ± 0.01	0.53 ± 0.01
−0.5–0.0	0.44 ± 0.01	0.46 ± 0.02	0.58 ± 0.03	0.04 ± 0.01	0.39 ± 0.01	0.47 ± 0.01
0.0–0.5	0.33 ± 0.02	0.27 ± 0.03	0.41 ± 0.10	0.00 ± 0.00	0.11 ± 0.01	0.30 ± 0.02
0.5–1.0	0.25 ± 0.05	0.47 ± 0.09	0.50 ± 0.35	0.00 ± 0.00	0.00 ± 0.00	0.11 ± 0.02
			Fit with Lognormal Distribution			
μ	-0.38 ± 0.03	-0.47 ± 0.03	-0.75 ± 0.03	-2.26 ± 0.07	-0.88 ± 0.03	-0.71 ± 0.03
σ	0.87 ± 0.02	0.87 ± 0.02	0.78 ± 0.02	1.39 ± 0.07	0.92 ± 0.02	0.74 ± 0.02
χ^2_ν	1.2	5.9	14.7	29.2	29.1	15.3

Notes.
[a] In units of (erg s^{-1}).

Table 9
Properties of Type 1 AGNs[a]

SDSS ObjID	R.A.[b] (degree)	decl.[b] (degree)	z	$\log L$[O III] (erg s^{-1})	$\mathrm{FWHM}_{bH\alpha}$ (km s^{-1})	$\mathrm{EW}_{bH\alpha}$ (Å)	$\log L_{bH\alpha}$ (erg s^{-1})	$\log(M_{BH}/M_{\odot})$[c]	$\log L_{bol}$[d] (erg s^{-1})	Notes[e]
587728309632106568	152.29813	2.74760	0.06319	39.98	6671.6 ± 89.2	56.9	41.18	$7.55^{+0.05}_{-0.05}$	43.52	*N*
587729229300760654	244.32758	52.48399	0.06319	39.85	3857.1 ± 159.1	18.6	40.77	$6.83^{+0.06}_{-0.05}$	43.40	*N*
587724648182448168	178.02454	−3.50442	0.06320	41.46	4120.9 ± 23.7	170.6	42.10	$7.62^{+0.05}_{-0.05}$	45.00	3
587732482763915309	229.21861	39.90373	0.06323	40.74	4606.0 ± 167.3	18.9	41.06	$7.15^{+0.06}_{-0.06}$	44.29	*N*
587742061069074446	175.31734	21.93939	0.06323	42.26	3850.9 ± 17.2	204.5	42.38	$7.72^{+0.06}_{-0.05}$	45.81	3
588295842853159031	156.47778	47.24015	0.06325	40.50	3736.5 ± 95.4	26.7	40.96	$6.91^{+0.05}_{-0.04}$	44.05	*XN*
587742188840943769	208.48332	21.99855	0.06333	40.39	6186.1 ± 101.2	41.7	41.34	$7.57^{+0.06}_{-0.06}$	43.93	*N*
587731522275311780	123.89431	35.28634	0.06337	40.75	3480.6 ± 39.1	64.5	41.36	$7.07^{+0.04}_{-0.04}$	44.29	3
587739097528270899	190.37257	37.36722	0.06340	41.26	4243.6 ± 32.3	118.5	41.84	$7.50^{+0.05}_{-0.05}$	44.81	3
588023668097875996	183.71655	19.01166	0.06340	40.37	4734.6 ± 75.3	57.1	41.19	$7.25^{+0.05}_{-0.04}$	43.91	3
587739827668844624	224.67809	21.60277	0.06343	38.78	2343.2 ± 9.9	243.0	42.18	$7.16^{+0.04}_{-0.04}$	42.32	3
587730847966888351	326.21548	0.47415	0.06344	40.62	3770.0 ± 83.4	34.5	40.89	$6.88^{+0.04}_{-0.04}$	44.17	*G*
587742060531089515	172.65646	21.23771	0.06347	40.14	4781.4 ± 149.6	24.6	40.99	$7.14^{+0.06}_{-0.05}$	43.68	*G*
587741720679612540	203.14915	25.29781	0.06353	39.93	4987.1 ± 99.6	52.1	41.23	$7.32^{+0.05}_{-0.05}$	43.48	*N*
587734690883698778	127.78179	5.35165	0.06356	40.93	4447.3 ± 65.3	55.8	41.34	$7.27^{+0.05}_{-0.05}$	44.48	3 *G*
587739721376792749	225.65990	24.22051	0.06361	41.11	4392.0 ± 43.7	92.6	41.42	$7.31^{+0.04}_{-0.04}$	44.66	3 *G*
587741600421314588	184.55672	26.40504	0.06361	40.21	2131.0 ± 20.9	70.4	41.17	$6.52^{+0.02}_{-0.02}$	43.75	3 *G*
588017977836765242	232.13504	28.96422	0.06362	40.72	4744.4 ± 64.9	61.1	41.42	$7.38^{+0.05}_{-0.05}$	44.27	*G*
587739810484650051	208.23201	25.48323	0.06366	41.30	2505.1 ± 14.0	175.1	41.84	$7.03^{+0.03}_{-0.03}$	44.84	3*HG*

Notes.
[a] This table is also available on the OSSY Web site (http://gem.yonsei.ac.kr/ossy/).
[b] J2000 coordinates.
[c] Black hole mass derived from the method developed by Greene & Ho (2005).
[d] Bolometric luminosity derived from the method developed by Heckman et al. (2004).
[e] Flag presenting the newly identified type 1 AGNs ("*N*") with the *Chandra* X-ray data ("*X*"). "3" indicates the SDSS *SpecClass* 3 objects. "*H*" and "*G*" indicate that the object was also identified by Hao et al. (2005) and Greene & Ho (2007), respectively.

(This table is available in its entirety in machine-readable form.)

only matched the stellar mass. Nevertheless, we can expect a general trend of star-formation-caused dilution of AGNs relying on the large-number statistics. The finding of new type 2 AGNs reduces the type 1 AGN fraction, especially in low-luminosity bins, but it seems clear that the current versions of the receding torus model still do not reproduce the "corrected" type 1 fraction.

We now attempt to find fits to our new data by adopting the general form of Simpson's formula, but treating α, L_0, and ξ as free parameters. We assume $\xi \geqslant 0$ because this condition is

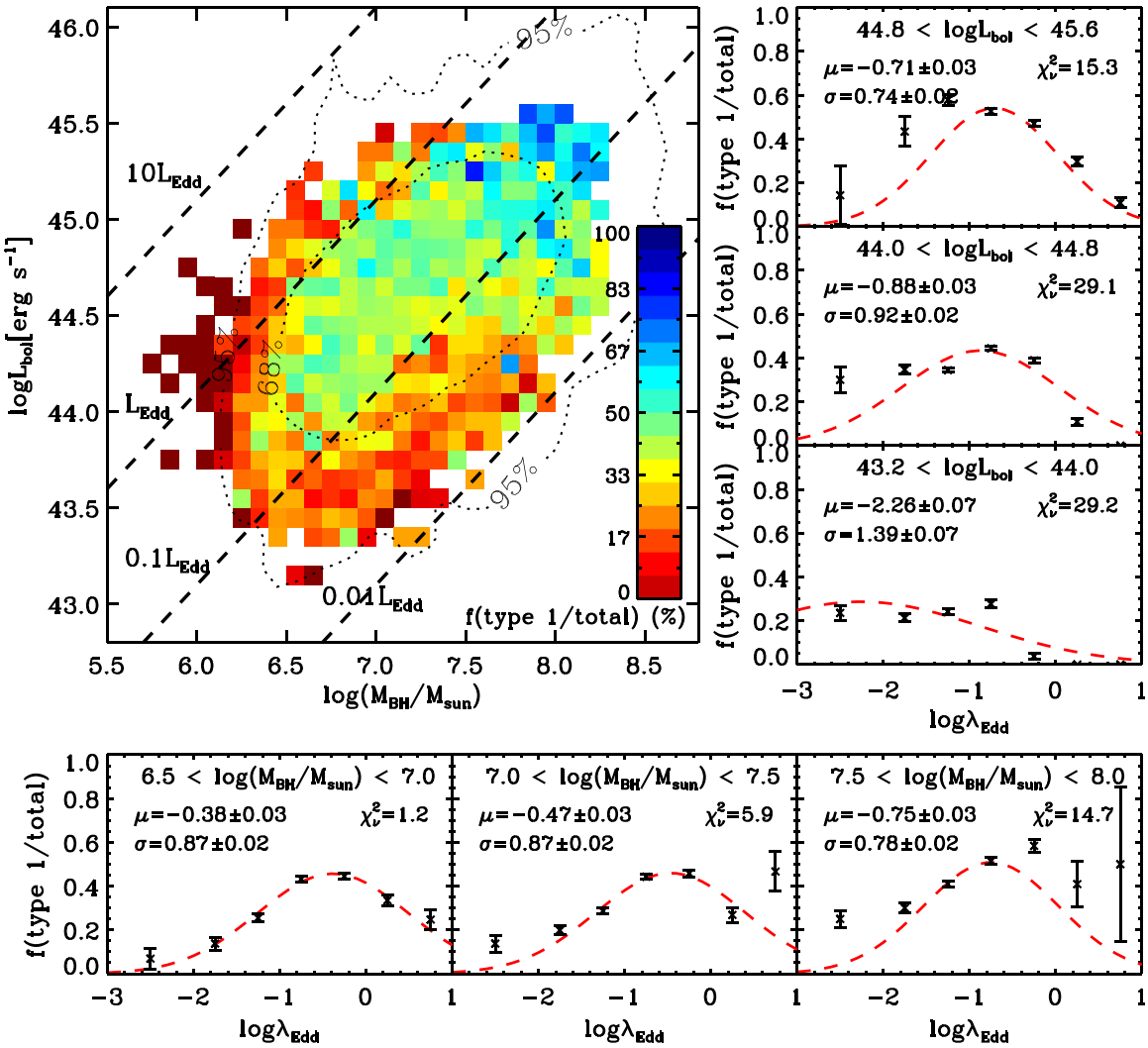

Figure 16. Type 1 AGN fraction with respect to bolometric luminosity and black hole mass. The main panel presents the type 1 AGN fraction using a color grid to denote bins including more than 10 objects in total (type 1 AGNs + type 2 AGNs). Black dotted curves indicate contours (68% and 95%) for type 1 AGNs, and dashed lines indicate various Eddington ratios. Right panels: Type 1 AGN fraction vs. Eddington ratio for various ranges of bolometric luminosity. Bottom panels: Type 1 AGN fraction vs. Eddington ratio for various ranges of black hole mass. Red curves in the right and bottom panels show lognormal fits. Table 8 lists all of the data points, errors, and fitting results.

essential to the receding torus model. The best fits were found with $\alpha = 0.12$, $L_0 = 39.7$, $\xi = 0.0$, and $\chi_\nu^2 = 6.6$ for the "observed" data set and with $\alpha = 0.14$, $L_0 = 40.1$, $\xi = 0.0$, and $\chi_\nu^2 = 8.3$ for the "corrected" data set. The new fits are shown as blue and red dashed lines in Figure 14. However, these two best fits have goodness-of-fit values (χ_ν^2) that are too large to accept and are much larger than that found by Simpson for the old data (1.5). In our test, χ_ν^2 became smaller with decreasing ξ. Our best fit was found with $\xi = 0$. This implies that the introduction of a "modification" (i.e., a positive luminosity dependence of torus height) seems unsupported. In fact, better fits were achieved with a negative value of ξ, but the improvement was marginal. The new data call for a new and improved explanation.

4. SUMMARY AND DISCUSSION

We have presented a process for finding new type 1 AGNs at $z < 0.2$ from the SDSS DR7 database. Adding the new type 1 AGNs (1835) to those in the previous database (3718) that also pass our selection criteria increases the size of the type 1 AGN database by 49%. Based on the new database, we calculated a new type 1 AGN fraction, which provides a useful test and constraint to our theoretical understanding of AGN geometry. We are pleased to release the spectroscopic properties of all type 1 AGNs, given in Table 9, and our calculations of the type 1 AGN fraction based on L[O III] and the Eddington ratio, given in Tables 7 and 8, respectively. It is our wish that these tables will be useful to the community.

We showed that our updated type 1 AGN fraction is not consistent with the current versions of the receding torus model. The type 1 AGN fraction in the low- and intermediate-luminosity bins is significantly higher than that given by previous data and models, even after correcting for dilution effects on emission lines caused by star formation. We found fits to the new data based on the basic formulation of the receding torus model, allowing large differences in the parameterization process, but these fits were poor. Thus, the new fits do not seem to support the hypothesis that torus depth depends on AGN luminosity.

We present the type 1 AGN fraction with respect to black hole mass and bolometric luminosity in Figure 16. We used the same bolometric correction factor, 3500, for both types of AGN

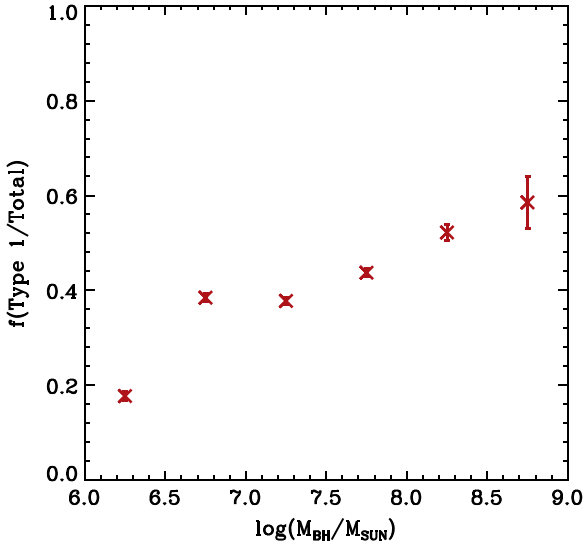

Figure 17. Type 1 AGN fraction with respect to black hole mass.

following Heckman et al. (2004). The bolometric correction factor may be uncertain; however, if there is no serious type bias, our results and conclusions in the relative sense would hold well. The color grids in the main panel of Figure 16 show that there is a favored area in which the type 1 AGN fraction is high for higher black hole mass and bolometric luminosity. This ridge-shaped distribution suggests that neither black hole mass nor bolometric luminosity solely determines the type 1 AGN fraction. Rather, the type 1 AGN fraction suggests a rising and falling distribution versus the Eddington ratio (see the small panels in Figure 16). If this trend is real, then it may imply that the opening angle initially widens with increasing Eddington ratio until the Eddington limit and diminishes thereafter, which is not expected based on the basic scheme of the receding torus model. Admittedly, however, the goodness of fit (χ_ν^2) is too poor to draw any definite conclusion at this time.

The structure of the dust torus is a key ingredient to understanding the AGN unification theory. However, its physical properties and detailed geometry are still under debate. Krolik & Begelman (1988) proposed that the dust and gas in the torus take the form of optically thick, self-gravitating clouds. A clumpy and obscuring torus requires a small volume filling factor and a sufficient scale height compared to the mean free path of clouds (Hönig & Beckert 2007). In the framework of a clumpy torus model, the largest clouds in the torus become gravitationally unbound from the high-luminosity AGN when the AGN accretes and radiates close to the Eddington limit. Based on this argument, the relationship $H/R \sim L^{-1/4}$ was derived, where H is the scale height, R is inner radius of the torus, and L is the AGN luminosity. Note that here the scale height inversely correlates with the AGN luminosity, unlike in the receding torus model. Elitzur & Shlosman (2006) described the origin of dust clouds as an outflow wind released from an accretion disk. Because outflow velocities are expected to decrease with R, the torus outflow scenario also predicts the luminosity dependence of the type 1 AGN fraction. Again, however, our data in Figure 16 do not seem to show a monotonic luminosity dependence. Instead, the covering factor of the torus seems to vary with the Eddington ratio, showing a favored spot in the black hole mass and bolometric luminosity diagram.

From the perspective of black hole mass, i.e., the horizontal axis of Figure 16, a smaller black hole mass regime shows a lower type 1 AGN fraction. It can clearly be seen in Figure 17 that the type 1 AGN fraction gradually increases with black hole mass. As lower-mass black holes allow more orbits close to their center, the accretion disk is more heated up over ionizing broad Hα emitting BLRs. However, it should be noted that further detailed analysis is required to confirm this interpretation.

It is also noteworthy that there have been discussions regarding the effect of the Eddington ratio and luminosity of AGNs on the presence of BLRs. Nicastro et al. (2003) presented evidence that hidden BLRs are found above a certain threshold value of Eddington ratio based on their earlier model (Nicastro 2000) and a handful of spectropolarimetric samples with X-ray data. They claimed that BLRs are formed by accretion disk instabilities, and the critical radius becomes smaller than the innermost stable orbit under low enough accretion rates. Similarly, Elitzur & Ho (2009) showed that type 1 AGNs are not found below a certain luminosity based on the disk-wind scenario. Their data support the disappearance of BLRs in the radiatively inefficient accretion regime, which is far lower than our data presented here.

In conclusion, our new type 1 AGN catalog seems to pose a serious challenge to the current favorite versions of the AGN unified model, but the improved database will hopefully help us to better understand the AGN classifications in the end.

We are grateful to the anonymous referee for a number of clarifications that improved the quality of the manuscript. K.O. acknowledges support from the Swiss Government Excellence Scholarship for the academic year 2013–2014 (ESKAS No. 2013.0308). S.K.Y acknowledges support from the National Research Foundation of Korea (Doyak 2014003730). S.K.Y acted as the corresponding author. K.S. and M.K. gratefully acknowledge support from the Swiss National Science Foundation Professorship grant PP00P2 138979/1, and M.K. acknowledges support from SNSF Ambizione grant PZ00P2 154799/1. This study was performed under the DRC collaboration between Yonsei University and the Korea Astronomy and Space Science Institute.

REFERENCES

Abazajian, K., Adelman-McCarthy, J. K., Agüeros, M. A., et al. 2004, AJ, 128, 502
Alonso-Herrero, A., Pérez-González, P. G., Rieke, G. H., et al. 2008, ApJ, 677, 127
Antonucci, R. 1993, ARA&A, 31, 473
Arnaud, K. A. 1996, in ASP Conf. Ser. 101, Astronomical Data Analysis Software and Systems V, ed. G. H. Jacoby & J. Barnes (San Francisco, CA: ASP), 17
Assef, R. J., Stern, D., Kochanek, C. S., et al. 2013, ApJ, 772, 26
Baldwin, J. A., Phillips, M. M., & Terlevich, R. 1981, PASP, 93, 5
Ballo, L., Cristiani, S., Fasano, G., et al. 2007, ApJ, 667, 97
Bruzual, G., & Charlot, S. 2003, MNRAS, 344, 1000
Burlon, D., Ajello, M., Greiner, J., et al. 2011, ApJ, 728, 58
Cappellari, M., & Emsellem, E. 2004, PASP, 116, 138
Cash, W. 1979, ApJ, 228, 939
Elitzur, M., & Ho, L. C. 2009, ApJL, 701, L91
Elitzur, M., & Shlosman, I. 2006, ApJL, 648, L101
Evans, I. N., Primini, F. A., Glotfelty, K. J., et al. 2010, ApJS, 189, 37
Fabian, A. C., Rees, M. J., Stella, L., & White, N. E. 1989, MNRAS, 238, 729
Falcke, H., Gopal-Krishna, & Biermann, P. L. 1995, A&A, 298, 395
Filippenko, A. V. 1997, ARA&A, 35, 309
Greene, J. E., & Ho, L. C. 2005, ApJ, 630, 122
Greene, J. E., & Ho, L. C. 2007, ApJ, 667, 131

Grimes, J. A., Rawlings, S., & Willott, C. J. 2004, MNRAS, 349, 503
Grimes, J. P., Heckman, T., Strickland, D., & Ptak, A. 2005, ApJ, 628, 187
Grimm, H.-J., Gilfanov, M., & Sunyaev, R. 2003, MNRAS, 339, 793
Haardt, F., & Maraschi, L. 1991, ApJL, 380, L51
Haggard, D., Green, P. J., Anderson, S. F., et al. 2010, ApJ, 723, 1447
Hao, L., Strauss, M. A., Fan, X., et al. 2005, AJ, 129, 1795
Hasinger, G. 2004, NuPhS, 132, 86
Hasinger, G. 2008, A&A, 490, 905
Heckman, T. M., Kauffmann, G., Brinchmann, J., et al. 2004, ApJ, 613, 109
Hill, G. J., Goodrich, R. W., & Depoy, D. L. 1996, ApJ, 462, 163
Hönig, S. F., & Beckert, T. 2007, MNRAS, 380, 1172
Huchra, J., & Burg, R. 1992, ApJ, 393, 90
Kauffmann, G., Heckman, T. M., Tremonti, C., et al. 2003, MNRAS, 346, 1055
Kawaguchi, T., Shimura, T., & Mineshige, S. 2001, ApJ, 546, 966
Kennicutt, R. C., Jr. 1998, ApJ, 498, 541
Kewley, L. J., Dopita, M. A., Sutherland, R. S., Heisler, C. A., & Trevena, J. 2001, ApJ, 556, 121
Krolik, J. H., & Begelman, M. C. 1988, ApJ, 329, 702
Lawrence, A. 1991, MNRAS, 252, 586
Lehmer, B. D., Alexander, D. M., Bauer, F. E., et al. 2010, ApJ, 724, 559
Maia, M. A. G., Machado, R. S., & Willmer, C. N. A. 2003, AJ, 126, 1750
Maiolino, R., & Rieke, G. H. 1995, ApJ, 454, 95
Markwardt, C. B. 2009, in ASP Conf. Ser. 411, Astronomical Data Analysis Software and Systems XVIII, ed. D. A. Bohlender, D. Durand, & P. Dowler (San Francisco, CA: ASP), 251
Mineo, S., Gilfanov, M., & Sunyaev, R. 2011, AN, 332, 349
Nicastro, F. 2000, ApJL, 530, L65
Nicastro, F., Martocchia, A., & Matt, G. 2003, ApJL, 589, L13
Oh, K., Sarzi, M., Schawinski, K., & Yi, S. K. 2011, ApJS, 195, 13
Osterbrock, D. E., & Shaw, R. A. 1988, ApJ, 327, 89
Peng, C. Y., Ho, L. C., Impey, C. D., & Rix, H.-W. 2002, AJ, 124, 266
Ranalli, P., Comastri, A., & Setti, G. 2003, A&A, 399, 39
Salim, S., Rich, R. M., Charlot, S., et al. 2007, ApJS, 173, 267
Sánchez, S. F., Jahnke, K., Wisotzki, L., et al. 2004, ApJ, 614, 586
Sánchez-Blázquez, P., Peletier, R. F., Jiménez-Vicente, J., et al. 2006, MNRAS, 371, 703
Sarzi, M., Falcón-Barroso, J., Davies, R. L., et al. 2006, MNRAS, 366, 1151
Schawinski, K., Thomas, D., Sarzi, M., et al. 2007, MNRAS, 382, 1415
Schawinski, K., Treister, E., Urry, C. M., et al. 2011, ApJL, 727, L31
Schawinski, K., Virani, S., Simmons, B., et al. 2009, ApJL, 692, L19
Schawinski, K., Urry, C. M., Virani, S., et al. 2010, ApJ, 711, 284
Schneider, D. P., Richards, G. T., Hall, P. B., et al. 2010, AJ, 139, 2360
Simmons, B. D., Lintott, C., Schawinski, K., et al. 2013, MNRAS, 429, 2199
Simmons, B. D., & Urry, C. M. 2008, ApJ, 683, 644
Simpson, C. 2005, MNRAS, 360, 565
Steffen, A. T., Barger, A. J., Cowie, L. L., Mushotzky, R. F., & Yang, Y. 2003, ApJL, 596, L23
Stern, J., & Laor, A. 2012, MNRAS, 423, 600
Ueda, Y., Akiyama, M., Ohta, K., & Miyaji, T. 2003, ApJ, 598, 886
Urry, C. M., & Padovani, P. 1995, PASP, 107, 803
Vanden Berk, D. E., Shen, J., Yip, C.-W., et al. 2006, AJ, 131, 84
Wachter, K., Leach, R., & Kellogg, E. 1979, ApJ, 230, 274
Westoby, P. B., Mundell, C. G., & Baldry, I. K. 2007, MNRAS, 382, 1541
Willott, C. J., Rawlings, S., Blundell, K. M., & Lacy, M. 2000, MNRAS, 316, 449
York, D. G., Adelman, J., Anderson, J. E., Jr., et al. 2000, AJ, 120, 1579
Zdziarski, A. A., Poutanen, J., & Johnson, W. N. 2000, ApJ, 542, 703